Fungal biofilm morphology impacts hypoxia fitness and disease progression

Caitlin H. Kowalski¹, Joshua D. Kerkaert¹, Ko-Wei Liu¹, Matthew C. Bond ⁰², Raimo Hartmann⁴, Carey D. Nadell ⁰², Jason E. Stajich ⁰³ and Robert A. Cramer ⁰^{1*}

Microbial populations form intricate macroscopic colonies with diverse morphologies whose functions remain to be fully understood. Despite fungal colonies isolated from environmental and clinical samples revealing abundant intraspecies morphological diversity, it is unclear how this diversity affects fungal fitness and disease progression. Here we observe a notable effect of oxygen tension on the macroscopic and biofilm morphotypes of the human fungal pathogen Aspergillus fumigatus. A hypoxia-typic morphotype is generated through the expression of a subtelomeric gene cluster containing genes that alter the hyphal surface and perturb interhyphal interactions to disrupt in vivo biofilm and infection site morphologies. Consequently, this morphotype leads to increased host inflammation, rapid disease progression and mortality in a murine model of invasive aspergillosis. Taken together, these data suggest that filamentous fungal biofilm morphology affects fungal-host interactions and should be taken into consideration when assessing virulence and host disease progression of an isolated strain.

urface-dwelling microorganisms organize into macroscopic colonies of intricately structured populations that have intrigued scientists for decades^{1,2}. For bacteria and yeast, the inter- and intraspecies heterogeneity of these macroscopic morphologies in vitro are well-understood^{3,4}; and microbial colony morphology (CM) variants are observed in clinical samples^{5,6}. The challenge remains to determine how CM diversity reflects physiological variation and contributes to environmental fitness. CM is associated with changes in extracellular matrix⁷, stress resistance⁸, reproduction⁹ and metabolism¹⁰; but it remains unclear, particularly for filamentous fungi, how CM affects pathogenesis and what genetic factors play a role in fungal CM diversification.

Intraspecies CM variation can arise through accumulated genetic changes or through transcriptional rewiring resulting in phenotypic switching^{11,12}. The human pathogenic mould *Aspergillus fumigatus* shows phenotypic plasticity at 0.2% O₂, where CM differs compared to that at 21% O₂ and is variable across strains¹³. Physiological changes and genetic mechanisms facilitating stable morphotype variants in *A. fumigatus* and other human pathogenic filamentous fungi are not well-characterized, nor is their effect on pathogenesis and disease progression. Progress in understanding fungal CM and phenotypic variability has been limited partly by the underlying genetic complexity. Given the intraspecies CM variation found in *A. fumigatus* isolates and the effect of oxygen on CM, we sought to assess how a low-oxygen CM variant affects *A. fumigatus* pathogenesis and invasive aspergillosis disease progression and to identify genetic factors involved in CM variation.

Results

Oxygen tension significantly influences fungal CM and biofilm architecture. A. fumigatus CM is heterogeneous in response to oxygen tension¹³. A screen of 58 isolates at 0.2% O₂ for two morphological features—colony furrowing and percentage vegetative mycelia (white, non-conidiating mycelia; PVM)—revealed abundant furrowing (mean, 5.30) and a high PVM (mean, 70.4%) (Fig. 1a and

Supplementary Fig. 1a). Colonies at 21% O_2 have significantly fewer furrows (mean, 1.85; P < 0.0001) and significantly reduced PVM (mean, 32%; P < 0.0001) (Fig. 1b). Oxygen tension is a significant source of variation for both colony furrowing (31.67%, P < 0.0001) and PVM (55.77%, P < 0.0001) (Fig. 1c,d). Most isolates screened have low furrowing and low PVM at normal oxygen (N-MORPH) and increased furrowing and PVM at low oxygen (hypoxia; H-MORPH; Fig. 1e). We consider a strain to be H-MORPH if furrows are greater than three and PVM is greater than 40% when grown in our culture conditions. A subset of clinical strains adopt H-MORPH even at 21% O_2 (filled circles, Fig. 1b–d,f). Three such strains—CDC20.2, F11698 and F16311—have significantly increased low oxygen fitness (H/N) relative to the N-MORPH reference AF293 (Fig. 1f and Supplementary Fig. 1b).

H-MORPH submerged fungal biofilms have altered biofilm architecture compared to AF293 (Fig. 1g). AF293 biofilms have a mat of filaments at the base perpendicular to the vertical axis. Above $\sim\!50\,\mu\text{m}$, filaments grow polarized toward the air–liquid interface with little deviation from the vertical axis (Fig. 1h and Supplementary Video 1). Clinical H-MORPH strains are similar in the first $\sim\!50\,\mu\text{m}$ but the remaining volume contains filaments that deviate from the vertical axis (Fig. 1h and Supplementary Fig. 2). This pattern of altered architecture is similar to AF293 cultured at 0.2% O_2 (Supplementary Video 2) and in the AF293 hypoxia-evolved H-MORPH strain EVOL20 independent of oxygen tension (Supplementary Videos 3 and 4, Fig. 1i,j and Supplementary Figs. 1c and 2). These data suggest that CM is an indicator of microscopic biofilm architecture affected by oxygen.

H-MORPH occurs throughout genetically diverse strains of *A. fumigatus*. H-MORPH is not segregated by clade in the *A. fumigatus* phylogeny (Supplementary Fig. 3). Two H-MORPH clinical strains—F11698/NCPF-7816 and F13611—represent the abundant *A. fumigatus* genetic diversity with one present in each of the two major clades (Supplementary Fig. 3). Genetically similar,

¹Department of Microbiology and Immunology, Geisel School of Medicine at Dartmouth, Hanover, NH, USA. ²Department of Biological Science, Dartmouth College, Hanover, NH, USA. ³Department of Microbiology and Plant Pathology and Institute for Integrative Genome Biology, University of California-Riverside, Riverside, CA, USA. ⁴Unaffiliated: Raimo Hartmann. *e-mail: Robert.A.Cramer.JR@Dartmouth.edu

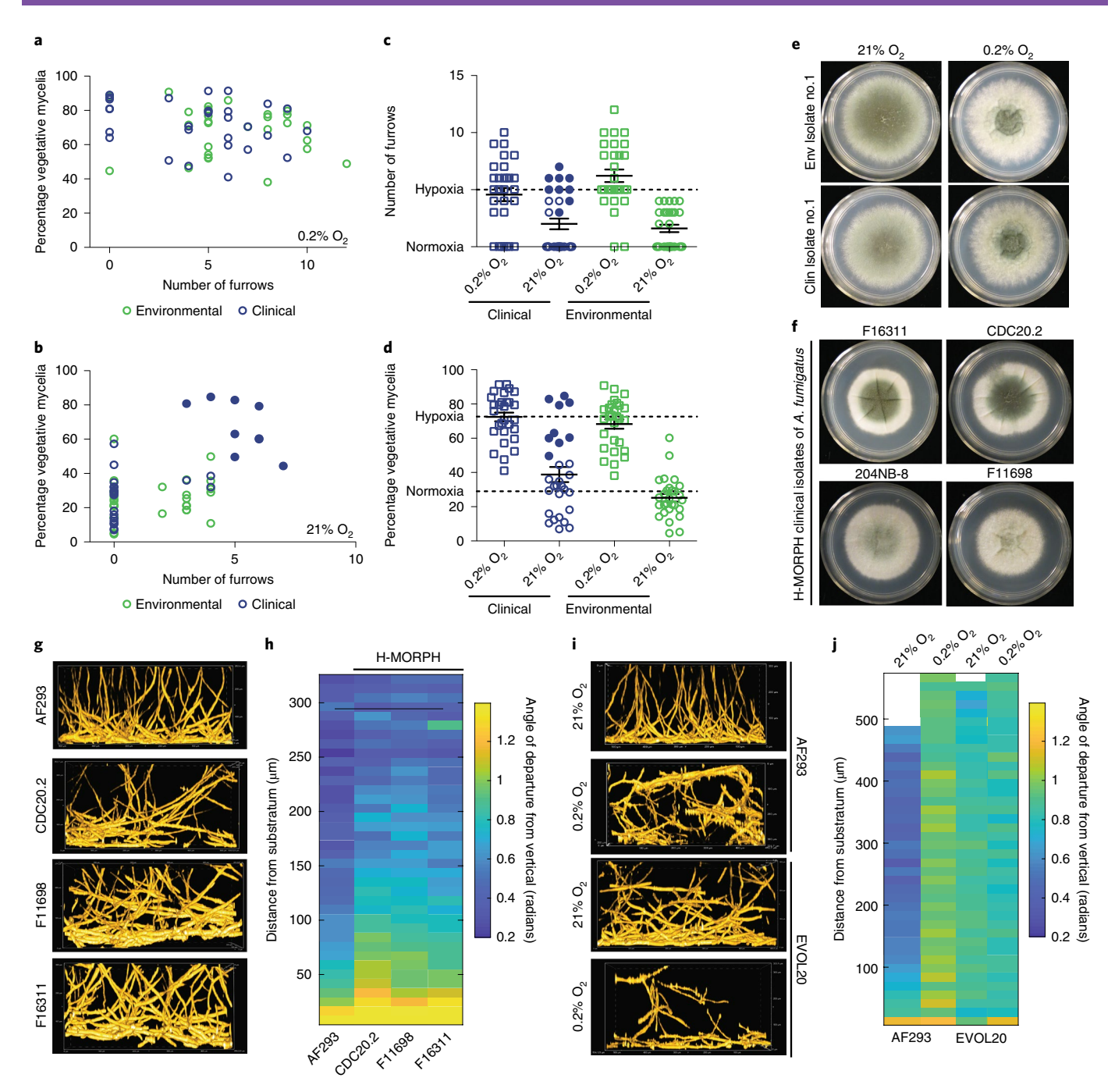


Fig. 1 | Macroscopic morphotypes and biofilm architecture of *A. fumigatus* are influenced by oxygen tension. a,b, Environmental (n=29 biologically independent samples) isolates of *A. fumigatus* strains plotted for morphotype characteristics (furrowing and percentage vegetative mycelia) when grown at 0.2% O_2 (a) or 21% O_2 (b). c,d, Two-way ANOVA shows oxygen tension significantly contributes to the variation of colony furrowing (31.67%, P<0.0001) (c) and PVM (55.77%, P<0.0001) (d) in clinical (n=29 biologically independent samples) strains. Dashed lines indicated the mean values per condition; error bars indicate s.e.m. (centre). e, Representative isolates with an increased PVM (white) and furrowing when cultured at 0.2% O_2 versus 21% O_2 . Images are representative of three biologically independent experiments. f, Example clinical strains that adopt H-MORPH during growth at 21% O_2 (closed blue circles in b, c and d). Images are representative of three biologically independent replicates. g, Representative side-view slices of submerged fungal biofilms from *A. fumigatus* H-MORPH clinical isolates in f. h, Quantification of vertical alignment of filaments as a function of biofilm depth. i,j Representative side-view slices of submerged fungal biofilms of AF293 and the H-MORPH EVOL20 at 21% O_2 (24h) and 0.2% O_2 (36h) (i) with vertical alignment quantification (j). For h and j each lane is a representative alignment from a minimum of three independent biological replicates. Biofilm images are sample volumes of approximately 300 μm (height) × 500 μm (length) × 200 μm (width) and represent a minimum of three biologically independent experiments.

co-isolated, clinical strains, IFM 59356-3 and IFM 59356-1, have H-MORPH and N-MORPH respectively (Supplementary Fig. 4a)⁶. Consistent with H-MORPH (Fig. 1g,h), IFM 59356-3 has a biofilm

with greater filament deviation from the vertical relative to its N-MORPH counterpart IFM 59356-1 (Supplementary Fig. 4b,c). The lack of clustering of H-MORPH in the phylogeny and the

ability to generate this CM suggest multiple genetic mechanisms probably exist through which $A.\ fumigatus$ evolves these morphological features.

A subtelomeric gene *hrmA* allele is sufficient to generate H-MORPH. An in vitro experimental evolution approach with AF293 in 0.2% O₂ generated the strain EVOL20 that adopts H-MORPH independent of oxygen tension (Supplementary Fig. 1c,d)¹³. Whole-genome sequence analysis of EVOL20 revealed three non-synonymous mutations compared to AF293 (Supplementary Table 1), including a missense mutation in an uncharacterized hypothetical protein Afu5g14900. This single nucleotide polymorphism (D304G) was only identified in H-MORPH EVOL20 from the passaged population (Supplementary Fig. 1f). RNA sequencing indicates that Afu5g14900 transcript is significantly increased in EVOL20 relative to AF293 in both normal (P=0.0002) and low-oxygen conditions (P<0.0001; Supplementary Fig. 1e). Due to the generation of H-MORPH in EVOL20, the gene Afu5g14900 is named hypoxia-responsive morphology factor A, *hrmA*.

In AF293, hrmA loss ($\Delta hrmA^{AF}$) does not alter in vitro CM in terms of furrowing and PVM, however, reconstitution of $\Delta hrmA^{AF}$ with the EVOL20 allele of hrmA ($hrmA^{R-EV}$) is sufficient to generate H-MORPH independent of oxygen tension (Fig. 2a,b). Allele $hrmA^{R-EV}$ has hypoxia fitness equivalent to EVOL20 (Fig. 2c). Conversely, hrmA loss in EVOL20 ($\Delta hrmA^{EV}$) results in a loss of H-MORPH during growth at 21% O₂ (Fig. 2a,b) and a reduction in hypoxia fitness (Fig. 2c). Similar to H-MORPH locked clinical isolates (Fig. 1g) and EVOL20, $hrmA^{R-EV}$ generates a biofilm with vertically misaligned filaments above the first ~50 µm (Fig. 2d,e). Loss of hrmA in EVOL20 restores AF293-like biofilm architecture (Fig. 2f,g). Thus, the hypoxia-evolved allele of hrmA is sufficient and necessary to generate H-MORPH in AF293 and EVOL20, respectively.

H-MORPH coincides with the initiation of the hypoxia transcriptional response at ambient oxygen tensions. RNA sequencing was used to visualize broad consequences of H-MORPH at normal- and low-oxygen tensions. Hierarchical clustering of the transcriptomes reveals H-MORPHs $hrmA^{R-EV}$ and $hrmA^{OE}$ (overexpression of the AF293 allele in AF293) cluster independently from N-MORPHs AF293 and $\Delta hrmA^{AF}$ (Supplementary Fig. 5). Of the differentially expressed transcripts between $hrmA^{R-EV}$ and AF293 in 21% and 0.2% O₂, 58% are oxygen-responsive genes in AF293 (Fig. 3a and Supplementary Table 3). The gene ontology functional categories GO:0016491 oxidoreductase activity (32/904) and GO:0005506 iron ion binding (7/142) are significantly enriched in the differentially expressed genes between $hrmA^{R-EV}$ and AF293 (Supplementary Table 2); two categories shown previously to be enriched during the hypoxia response 14.

Transcripts with an increase or decrease of at least fourfold between AF293 and hrmA^{R-EV} were categorized as 'hypoxia-induced genes' (H/N > 4), 'hypoxia-reduced genes' (H/N < -4) or 'hypoxia non-responsive genes' (4 > H/N < -4) (Supplementary Table 4). At 21% O₂, 51% of the transcripts increased in hrmA^{R-EV} compared to AF293 are hypoxia-induced genes; conversely, 45% of the transcripts reduced in hrmA^{R-EV} compared to AF293 are hypoxia-reduced genes (Fig. 3b). Thus, H-MORPH strains, mediated by hrmA, activate the transcriptional hypoxic response despite oxygen replete conditions. At 0.2% O₂ where hrmA^{R-EV} is more fit than AF293, 71.8% of increased transcripts are hypoxia-reduced transcripts, further supporting an altered physiological response to hypoxic stress in H-MORPH strains (Fig. 3b). The inverted hypoxia response of hrmAR-EV coincides with reduced fungal biomass at 21% O2 and increased biomass at 0.2% O2 (Fig. 3c). However, following a shift from ambient oxygen to low oxygen the H-MORPH hrmAR-EV has increased growth rate compared to the N-MORPH AF293 (Fig. 3d).

HrmA is induced during murine pulmonary aspergillosis and facilitates the expression of a subtelomeric gene cluster. Previous reports suggest increased hrmA expression in vivo in a triamcinolone murine model of invasive aspergillosis¹⁵. In that model, hrmA transcript levels significantly increase from 24 to 72 h after fungal inoculation (Fig. 4a). An increase in hrmA transcript in hrmA^{R-EV} (at the native locus) is also observed (Fig. 4b). The allele hrmA is a member of a subtelomeric gene cluster that responds to nitrogen starvation, a laboratory condition that transcriptionally correlates with a host-adaptation transcriptional response¹⁶. Consistent with the assignment of hrmA to a subtelomeric gene cluster, we observe an influence of hrmA on transcript levels of genes surrounding its native locus, termed here the hrmA-associated cluster (HAC). In $\Delta hrmA^{EV}$, the messenger RNA levels of three surrounding genes (Afu5g14880, Afu5g14890 and Afu5g14910) are significantly reduced compared to EVOL20 (Fig. 4c). Ectopic overexpression of the AF293 allele of hrmA (hrmA^{OE}) acts in trans to facilitate an increase in transcripts of four HAC genes (Afu5g14880, Afu5g14890, Afu4g14910 and Afu5g14920; Fig. 4d).

Analysis of co-regulated transcripts from RNA sequencing predicts that HAC extends from Afu5g14865 to Afu5g14920 and includes a putative unannotated ORF 3' to Afu5g14910 (Supplementary Fig. 6a,c). The average gene size and percentage GC content of HAC is not different from the AF293 genomic average (Supplementary Fig. 6b)17; but in the hypoxia-fit strain A1163 (ref. 13), there is a subtelomeric HAC that is syntenic to AF293 HAC and two additional putative homologous clusters that are not present in AF293 (Supplementary Fig. 6c). The presence of these potential homologous clusters in a distantly related A. fumigatus strain suggests intragenomic movement of this genomic region. The clusters share certain genic components including genes encoding a MyB/SANT domain, a kinase domain, a DUF2841 domain and putative hrmA paralogs (hrmB, AFUB 044390; hrmC, AFUB 096600). Analysis of HAC across sequenced strains indicates heterogeneous abundance of the original and homologous gene clusters (Supplementary Fig. 3, alignment: https://github.com/ stajichlab/Afum_hrmA_cluster_evolution; https://doi.org/10.5281/ zenodo.3257606), potentially highlighting a role for these homologous clusters in H-MORPH generation where HAC is absent. Other Ascomycetes encode genes similar to hrmA, including the human fungal pathogens Histoplasma capsulatum and Coccidioides immitis (Supplementary Table 7; https://github.com/stajichlab/Afum_ hrmA_cluster_evolution).

HrmA nuclear localization is necessary for the induction of **HAC.** The HrmA protein sequence reveals a predicted N-terminal bipartite nuclear localization signal (http://nls-mapper.iab.keio. ac.jp/) and a weakly predicted RNA recognition motif domain (E-value, 0.01) (Supplementary Fig. 7a). Overexpression of the parental allele of *hrmA* with a C-terminal green fluorescent protein (GFP) tag in AF293 generates oxygen-independent H-MORPH (Fig. 4e,f). In contrast, overexpression of hrmA with a disrupted nuclear localization signal is unable to generate H-MORPH (Fig. 4e,f) despite increased levels of hrmA transcript (Fig. 4i). Confocal imaging reveals GFP signal enriched in the same location as the nuclear DAPI stain for the WT (wild type, AF293) allele but a lack of this enrichment for the nuclear localization signal mutant (Fig. 4g,h). Without localization to the nucleus or nuclear region, HrmA is unable to facilitate HAC induction as shown by the cluster gene cgnA (Afu5g14910) (Fig. 4i).

Despite low sequence similarity in the alignment to the RNA recognition motif domain in HrmA, there are two conserved phenylalanine residues in this domain that are also present in *hrmB* and *hrmC* in strain A1163. When these conserved phenylalanine residues are each mutated to alanine, overexpression of this allele cannot generate H-MORPH despite observing *hrmA* nuclear region

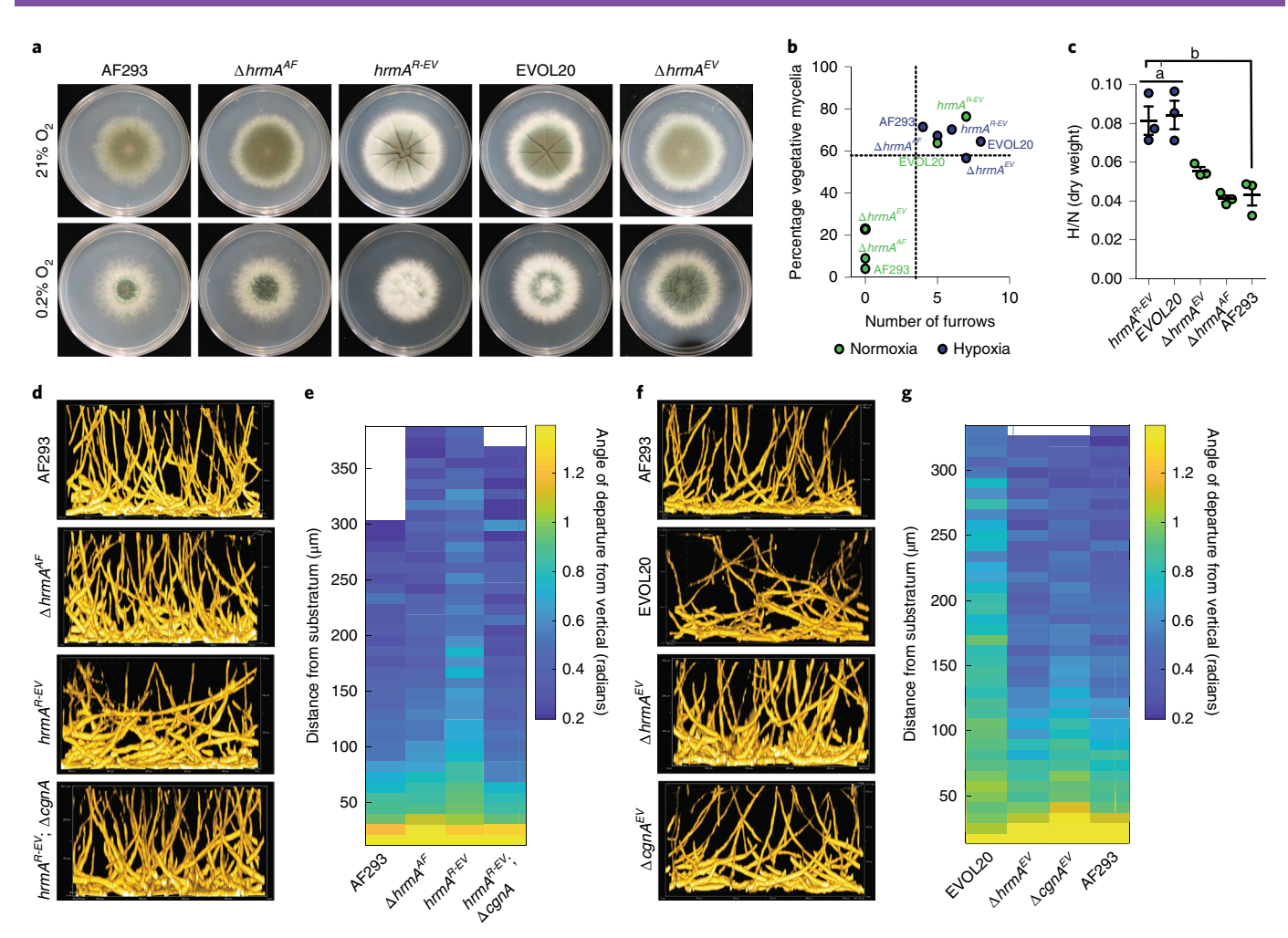


Fig. 2 | The hypoxia-evolved allele of the subtelomeric gene *hrmA* is sufficient to generate H-MORPH and collapse biofilm architecture. **a**, A hypoxia-evolved allele of *hrmA*, from the hypoxia-evolved strain EVOL20, is sufficient to generate H-MORPH in AF293 ($hrmA^{R-EV}$) and necessary for H-MORPH in EVOL20. Images are representative of three biologically independent experiments. **b**, Morphotype quantification indicates that $hrmA^{R-EV}$ and EVOL20 are above the mean (dashed lines) for furrowing and PVM, regardless of oxygen tension but dependent on hrmA/cgnA. **c**, Allele $hrmA^{R-EV}$ (n=3 biologically independent samples per group) has increased fitness (a, P=0.9942; b, P=0.0033 by one-way ANOVA with Tukey's multiple comparison test) in low oxygen as determined by dry weight. Error bars indicate s.e.m. (centre). **d.e**, Representative side-view slices of submerged fungal biofilms reveal that altered biofilm architecture in $hrmA^{R-EV}$ is dependent on cgnA as shown in **d** and quantified in **e**. **f**,**g**, Representative side-view slices of submerged fungal biofilms revealing that hrmA and cgnA are necessary for the collapse in biofilm architecture observed with EVOL20 as shown in **f** and quantified in **g**. Colony and biofilm analysis are representative of three biological replicates. Biofilm images are sample volumes of approximately 300 μm (height) × 200 μm (width).

localization (Supplementary Fig. 7b–d). Aromatic residues are critical in many RNA recognition motif protein structures for direct interaction with nucleic acids¹⁸. Further studies are needed to determine the molecular function of *hrmA* in fungi.

H-MORPH is generated through HrmA-mediated induction of HAC. Loss of HAC induction abolishes H-MORPH indicating that HAC is necessary for this morphotype and increased hypoxia fitness (Fig. 5 and Supplementary Fig. 7). Expression of the HAC gene Afu5g14910, cgnA, is an indicator of HrmA downstream effects and encodes a predicted collagen-like protein, a class of proteins present but unstudied in other fungi (Supplementary Table 5). In A. fumigatus, CgnA has a tripeptide G-X-Y repeat of G-Q-I and G-Q-S and lacks a canonical secretion signal. Despite induction of cgnA greater than 100-fold relative to AF293 in hrmA^{OE} (Fig. 4d; morphology Supplementary Fig. 8e), comparative levels of cgnA overexpression in the absence of increased hrmA

(cgnA^{OE}) does not induce H-MORPH nor alter the hypoxic growth of AF293 (Supplementary Fig. 8). Loss of cgnA in the context of increased HAC abolishes H-MORPH, indicating a role for cgnA and possibly other HAC genes, in the generation of H-MORPH (Fig. 5a,b and Supplementary Fig. 8e). Loss of cgnA in HAC-induced strains EVOL20 and hrmA^{R-EV} reduces the hypoxia fitness of these strains (Fig. 5c and Supplementary Fig. 8f) and restores the N-MORPH biofilm architecture and filament alignment to that of AF293 (Fig. 2).

To further characterize the role of *cgnA* and HAC in the generation of H-MORPH, we assessed features of the hyphal surface, as surface alteration and adhesion are associated with other microbial collagen-like proteins^{19–21}. Loss of *cgnA* and regeneration of N-MORPH increases surface adherence of H-MORPH strains (Fig. 5d), probably the consequence of extracellular matrix detachment from the H-MORPH strains (Supplementary Fig. 8g and Fig. 5e) that is dependent on *cgnA*. In the clinical strains IFM 59356-1

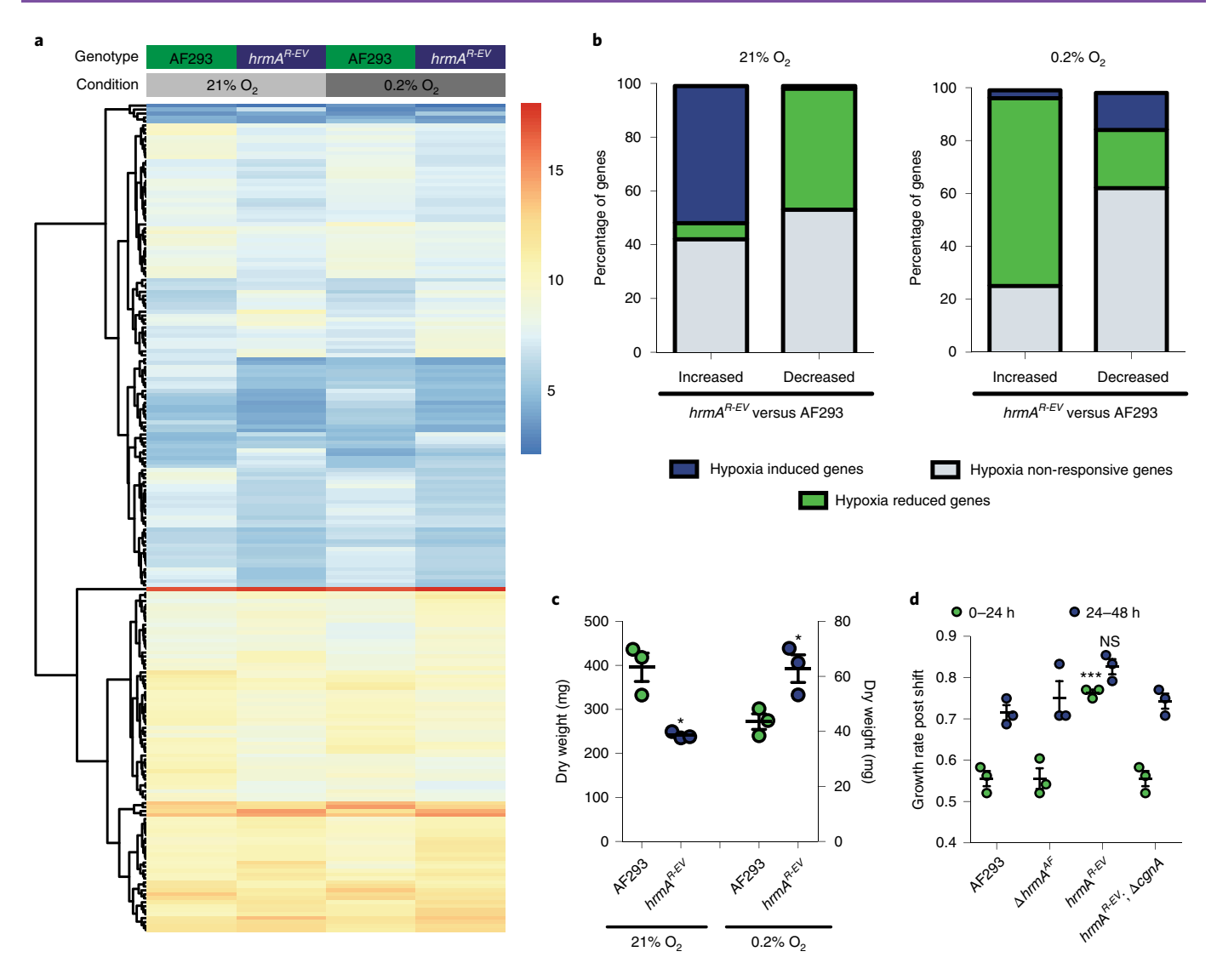


Fig. 3 | Transcriptional rewiring of the hypoxia response is dependent on the hypoxia-evolved allele of *hrmA* and primes for improved growth in low oxygen. **a**, A heat map of collapsed biological replicates showing top genes with P < 0.05 (two-sided) and \log_2 differential expression >1 with a minimum FPKM of 5. Significance was determined with DESeq2 which uses the Wald test for differential expression and adjustments for multiple comparisons using Benjamini and Hochberg procedures. In this subset, *hrmA*^{R-EV} versus AF293 reveals large-scale changes in both 21% and 0.2% O_2 as a result of the hypoxia-evolved *hrmA* allele. **b**, Classification of all genes increased or decreased twofold in *hrmA*^{R-EV}/AF293 at 21% O_2 or 0.2% O_2 reveals activation of the hypoxia transcriptional response at ambient oxygen and reduction in this response at low oxygen in *hrmA*^{R-EV}. **c**, The growth advantage of *hrmA*^{R-EV} at 0.2% O_2 (*P = 0.0282) coincides with a significant (*P = 0.0088) reduction in fungal growth at 21% O_2 . Two-tailed unpaired *t*-test performed on n = 3 independent biological replicates with error bars showing s.e.m. (centred). **d**, A transition from 48 h of growth at 21% O_2 to growth at 0.2% O_2 shows an initial increase (***P < 0.0001) in growth rate during the first 24 h at 0.2% O_2 for *hrmA*^{R-EV} that is not present (NS, P = 0.0789) 24-48 h after shift to 0.2% O_2 . One-way ANOVA with Tukey's multiple comparison test was performed on n = 3 biologically independent samples. Error bars indicate s.e.m. (centre); NS, not significant.

(N-MORPH) and IFM 59356-3 (H-MORPH), matrix detachment and reduced surface adherence is observed in H-MORPH relative to the N-MORPH (Supplementary Fig. 4d,e). Matrix detachment from the H-MORPH filaments is not a defect in extracellular matrix production as it is still visibly secreted into the biofilms (Fig. 5e). A significant component of the extracellular matrix is galactosaminogalactan (GAG) and loss of GAG through deletion of the UDP-glucose-4-epimerase uge3 abolishes surface adherence chemical modifications of GAG also prevents attachment of matrix to the hyphae²³, so we investigated the ability of secreted GAG from $hrmA^{OE}$ to complement the adherence defect of the GAG-deficient strain $\Delta uge3^{AF}$. Culture supernatants containing secreted GAG from AF293 and $hrmA^{OE}$ were both able to significantly increase adherence of $\Delta uge3^{AF}$ (Fig. 5f). These data suggest

that HAC/cgnA modifies the hyphal surface mediating matrix/ GAG detachment. To determine if GAG secretion was necessary for H-MORPH, we generated *uge3* deletions in *hrmA*^{OE} and EVOL20; as a result, CM did not change but surface adherence was abolished (Supplementary Fig. 9a,b). Loss of GAG production in AF293 does not affect hypoxia fitness nor the biofilm architecture (Supplementary Fig. 9d,e).

H-MORPHs $hrmA^{R-EV}$ and EVOL20 have significantly thinner cell walls than the N-MORPH AF293 and in EVOL20 this is dependent on cgnA (Fig. 5g and Supplementary Fig. 10). To determine if the cell wall architecture is altered, we imaged cell wall components through the use of calcofluor white (CFW) stain for chitin detection and soluble Dectin-1 for β-glucan detection²⁴. H-MORPH $hrmA^{R-EV}$ has reduced total chitin that is dependent on the induction

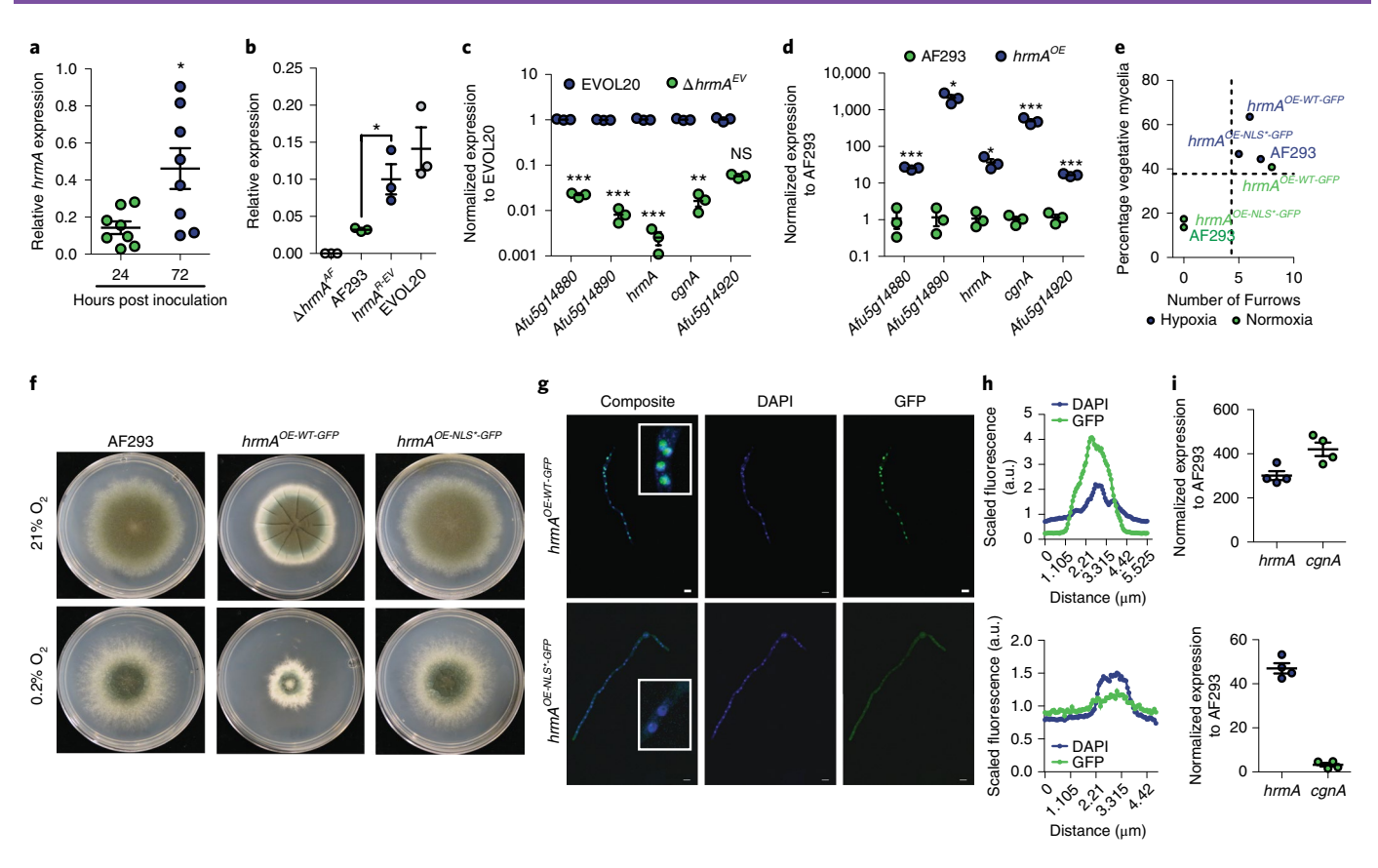


Fig. 4 | HrmA localizes to the nucleus where it facilitates induction of a subtelomeric gene cluster. **a**, Allele *hrmA* transcripts are detected in vivo during murine invasive disease with WT *A. fumigatus* and increase in abundance from 24 to 72 h after inoculation (n=8 biologically independent animals, unpaired two-tailed Students t-test, *P=0.0151). **b**, Introduction of the evolved allele of *hrmA* ($hrmA^{R-EV}$) is sufficient to induce significantly increased mRNA levels of *hrmA* compared to AF293 (*P=0.0290) and similar to EVOL20 (P=0.3066) (n=3 biologically independent samples). Students unpaired two-tailed t-test performed, error bars indicate s.e.m. (centre). **c**, In the hypoxia-evolved EVOL20, loss of *hrmA* leads to a significant reduction in mRNA for the gene cluster surrounding the *hrmA* native locus (HAC) (n=3 biologically independent samples). Unpaired Students two-tailed t-test performed between EVOL20 and $\Delta hrmA^{EV}$ with error bars representing s.e.m. (centre) (Afu5g14880, ***P<0.0001; Afu5g14890, ***P<0.0001; *hrmA* in AF293 acts in trans to significantly increase mRNA levels HAC (n=3 biologically independent samples). Unpaired Students two-tailed t-test performed between AF293 and $hrmA^{OE}$ with error bars representing s.e.m. (centre) (Afu5g14880, ***P=0.0018; hrmA, *hrmA, *hrm

of cgnA (Fig. 5h and Supplementary Fig. 11a). In contrast, $hrmA^{R-EV}$ has significantly increased cgnA-dependent β-glucan exposure (Fig. 5i and Supplementary Fig. 11b). Allele $hrmA^{R-EV}$ is also more sensitive to growth on CFW in both normal and low oxygen compared to AF293, $\Delta hrmA^{AF}$ and $hrmA^{R-EV}$; $\Delta cgnA$ (Supplementary Fig. 11c). No difference in sensitivity to the β-glucan synthase inhibitor caspofungin was observed (Supplementary Fig. 11d). We propose that these surface changes alter matrix attachment and inter-hyphal interactions in the developing biofilms resulting in a loss of vertically aligned polarized growing filaments.

H-MORPH altered biofilm architecture occurs in vivo. We next sought to determine if the altered filament surface influences the inter-filament interactions in vivo. We adopted the miPACT/PACT tissue-clearing methods (microbial identification after passive clarity technique) to visualize in vivo fungal lesions in three dimensions using fluorescently labelled fungi (we term this technique funPACT: fungal imaging after passive clarity technique)^{25–27}. At 4 days post inoculation (d.p.i.) and 5 d.p.i. large inflammatory foci

with fungal elements are observed in the airways of animals challenged with AF293 or EVOL20. At both time points, AF293 lesions are dense at the centre with filaments radiating from the foci of infection, becoming less dense away from the centre (Fig. 6a and Supplementary Video 5). There is a high degree of connectivity between filaments in AF293 lesions but not in EVOL20 lesions. At 4 d.p.i. and 5 d.p.i. the EVOL20 lesions are visibly more diffuse than those of AF293 (Fig. 6a,b and Supplementary Fig. 13). There are no dense foci in the EVOL20 lesions and single filaments can be observed dispersed in distinct locations in the mass of host immune infiltrate (Fig. 6b and Supplementary Video 6).

To quantify differences in lesion architecture, we performed Gömöri methenamine silver stain and applied a nearest-neighbour algorithm to quantify the 'compactness' of fungal lesions in the large airways. The more compact a fungal lesion is, the shorter the distance between each filament and its nearest neighbours; while more diffuse lesions have larger average distances between filaments. Qualitative analysis of the histopathology between N-MORPH AF293 and H-MORPH EVOL20 supported the hypothesis that

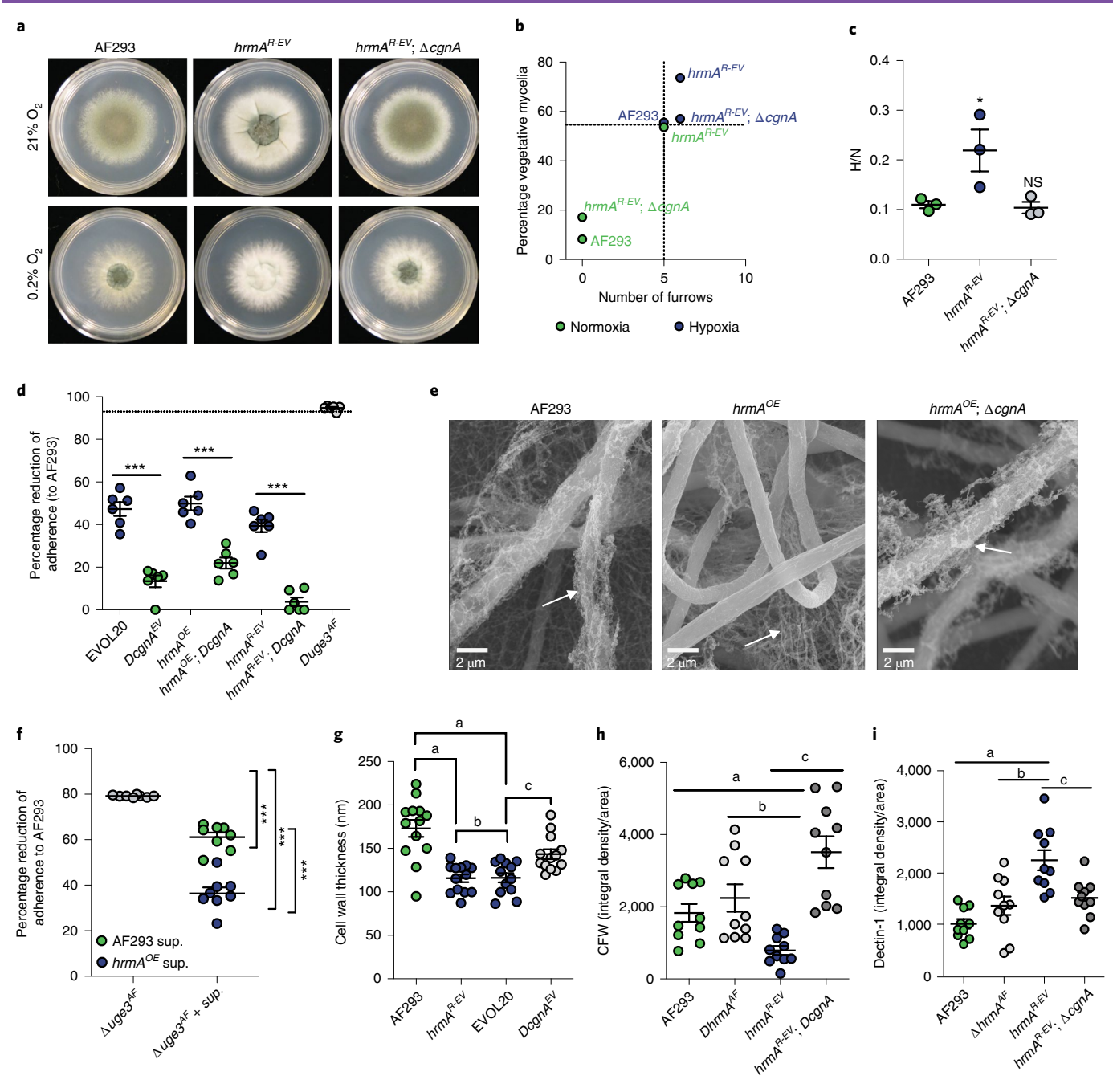


Fig. 5 | HrmA-facilitated induction of the surrounding subtelomeric gene cluster leads to increased hypoxia fitness and a modified hyphal surface. a,b, In a minimum of three independent experiments, loss of cgnA in $hrmA^{R+EV}$ abolishes H-MORPH (a) generating a AF293-like oxygen-responsive morphotype in regards to furrows and PVM (b). c, Representative HAC gene cgnA is necessary for the increased hypoxia fitness of $hrmA^{R+EV}$ (n=3 biological independent samples, one-way ANOVA with Dunnett's multiple comparison test, *P=0.0433 and NS P=0.9847). d, Adherence to plastic is reduced in response to HAC induction (EVOL20, $hrmA^{OE}$, $hrmA^{R+EV}$) and is dependent on cgnA. Biologically independent biological samples (n=6) are from two independent experimental repetitions. One-way ANOVA with Sidak's multiple comparison test performed, ***P<0.0001. Error bars indicate s.e.m. (centre). e, SEM of 24 h submerged fungal biofilms reveal detachment of extracellular matrix from $hrmA^{OE}$ hyphae that is dependent on cgnA. White arrows indicate extracellular matrix. Images are representative of three replicates. f, Addition of culture supernatants with secreted extracellular matrix to the non-adherent strain $\Delta uge3^{AF}$ significantly (****P<0.0001) rescues adherence. Biologically independent samples (n=8) with one-way ANOVA with Tukey's multiple comparison test. Error bars indicate s.e.m. (centre). g, The cell walls of $hrmA^{R-EV}$ and EVOL20 are significantly (a, P<0.001; b, P>0.9999; c, P=0.0034) thinner than those of AF293 or $\Delta cgnA^{EV}$. Independent biological samples (n=13) with one-way ANOVA and Tukey's multiple comparisons test. Error bars indicate s.e.m. (centre). h, h, $hrmA^{R-EV}$ has reduced total chitin staining by CFW fluorescence (n=10 independent biological samples; a, P=0.0049; b, P=0.0049; c, P<0.0001) (h) and increased β -glucan staining by Dectin-1 (n=10 independent biological samples; a, P<0.0001; b, P=0.0006; c, P=0.0044) (i). One-way ANOVA wi

H-MORPH fungal lesions are more diffuse and quantification reveals significantly less compact lesions with EVOL20 than AF293 (Fig. 6c). Expansion of this algorithm to lesions of N-MORPHs

 $\Delta hrmA^{AF}$ and $hrmA^{R-EV}$; $\Delta cgnA$ and H-MORPH $hrmA^{R-EV}$ reveal significantly reduced compactness of $hrmA^{R-EV}$ compared to the N-MORPH strains (Fig. 6c and Supplementary Figs. 12 and 13c).

The diffuse nature of the $hrmA^{R-EV}$ lesion is dependent on cgnA and only coincides with H-MORPH.

H-MORPH facilitate disease progression. H-MORPH F11698 (Supplementary Fig. 4h) (n=7) is significantly increased in murine virulence relative to AF293 $(n=5;\ P=0.0096;\ Supplementary$ Fig. 4i). However, these are non-isogenic strains with an estimated 35,759 single nucleotide polymorphisms between them that could contribute to differences in virulence and morphology. A second comparison between closely related clinical isolates N-MORPH IFM 59356-1 and H-MORPH IFM 59356-3 reveals a 40% increase in survival at 14 d.p.i. and a 5-d delay before the first mortality event in N-MORPH inoculated animals. By quantitative real-time polymerase chain reaction (qRT-PCR) no significant difference in mRNA levels of hrmA or the HAC gene cgnA is observed between these two strains that contain 51 non-synonymous single nucleotide polymorphisms between them (Supplementary Fig. 4g).

Loss of hrmA in AF293 does not affect murine mortality, however introduction of the hypoxia-evolved allele of hrmA ($hrmA^{R-EV}$) and generation of H-MORPH significantly augments virulence in a cgnA-dependent manner (Fig. 6d). Loss of hrmA or cgnA in the H-MORPH EVOL20 significantly attenuates EVOL20 virulence (Fig. 6e). Despite the H-MORPH strains increased virulence, there is no significant difference in fungal burden between AF293, $hrmA^{R-EV}$, $\Delta hrmA^{AF}$ and $hrmA^{R-EV}$; $\Delta cgnA$ at 4 d.p.i. (Fig. 6f). Increased β -glucan exposure in the cell wall of H-MOPRH strains is consistent with observed increases in inflammation at 4 d.p.i. (Fig. 6g and Supplementary Fig. 1h,i). The airways where H-MORPH $hrmA^{R-EV}$ is growing are full of immune cell infiltrate that is reduced around lesions of N-MORPH strains (Fig. 6g).

Host cell damage measured through lactate dehydrogenase (LDH) release in bronchoalveolar lavage fluid (BALF) after inoculation with hrmAR-EV indicates a significant increase in host cell damage (Fig. 6h). In both the airways and lung tissue, H-MORPH inoculum is associated with a significant increase in total cells (Supplementary Fig. 14a,e) and CD45+ leucocytes (Supplementary Fig. 14b,f). A significant increase in the neutrophil chemoattractant KC from BALF is detected (Fig. 6i) and corresponds with an increase in airway neutrophils (Fig. 6j). The elevated host response to inoculation with H-MORPH hrmA^{R-EV} is dependent on HAC/cgnA, as loss of cgnA does not reduce hrmA transcripts (Supplementary Fig. 14h). These data indicate that localized pulmonary inflammation is increased following inoculation with H-MORPH; but in addition, systemic inflammation, as measured by spleen weight, is significantly increased 60 h after fungal inoculation with hrmA^{R-EV} compared to AF293, $\Delta hrmA^{AF}$ and $hrmA^{R-EV}$; $\Delta cgnA$ (Fig. 6k). Together, these data suggest H-MORPH occurs in vivo and significantly affects disease progression in part through an increase in immunopathogenesis.

Discussion

While morphological heterogeneity has been reported among filamentous fungi^{6,13,28,29}, there is an existing gap in knowledge that links CM with specific genetic determinants and disease outcomes. Here we discover an oxygen-mediated mechanism of A. fumigatus CM that is associated with increased disease progression and fungal virulence. H-MORPH CM leads to increased hypoxia fitness and enhanced virulence through alterations in fungal biofilm architecture that promote increased host inflammation. It remains an open question how H-MOPRH confers a fitness benefit during low-oxygen growth on a population scale and, on the microscale, how the coinciding altered biofilms affect oxygen metabolism of individual filaments. Colony wrinkling or rugose CM has been characterized in a number of microorganisms, including Candida albicans, where increased oxygen penetration is observed in wrinkles³⁰. Further investigation is necessary to address how the morphotype variant H-MORPH confers increased hypoxia fitness.

Our studies identified a subtelomeric gene cluster probably regulated by the gene hrmA that is sufficient to drive H-MORPH when expressed (Supplementary Fig. 15). This cluster of genes is interesting independent of its facilitation of H-MORPH for more reasons including: (1) its location in the subtelomeric region¹⁶, (2) its mysterious origin and strain-dependent putative duplications (Supplementary Fig. 6), (3) its strain-specific occurrence across the A. fumigatus phylogeny (Supplementary Fig. 3) and (4) its genic content (Supplementary Fig. 6). Genetic variation in the cluster genes (Afu5g14865 and Afu5g14920) has also been observed in clinical strains²⁸. The evolutionary history of HAC and the putative homologous gene clusters and their molecular functions remains an intriguing area of future study. However, the isogenic set of morphotype variants generated here will serve as tools to continue to interrogate the physiological consequences of CM on A. fumigatus pathogenesis. Understanding how fungal macroscopic morphotypes reflect in vivo phenotypic changes in human fungal pathogens may allow for morphotype indicators of disease progression and advancement of patient care.

Methods

Strains and growth conditions. *A. fumigatus* AF293 was used in the published experimental evolution approach that generated EVOL20 (ref. ¹³). Mutant strains were generated in AF293, the uracil/uridine auxotroph AF293.1 or EVOL20 (Supplementary Table 6). IFM 59356-1 and IFM 59356-3 were provided by D. Hagiwara⁶. Strains were cultured as described on 1% glucose minimal media (GMM)³¹ and collected for experimentation as previously described³¹.

Strain construction. Strain genotypes are provided in Supplementary Table 6. Gene replacement mutants were generated as previously described using overlap extension PCR 32. The *hrmA*-GFP alleles were constructed through overlap extension PCR to tag HrmA at the C terminus. Site-directed mutation of *hrmA* was carried out using QuikChange Site-Directed Mutagenesis (Agilent).

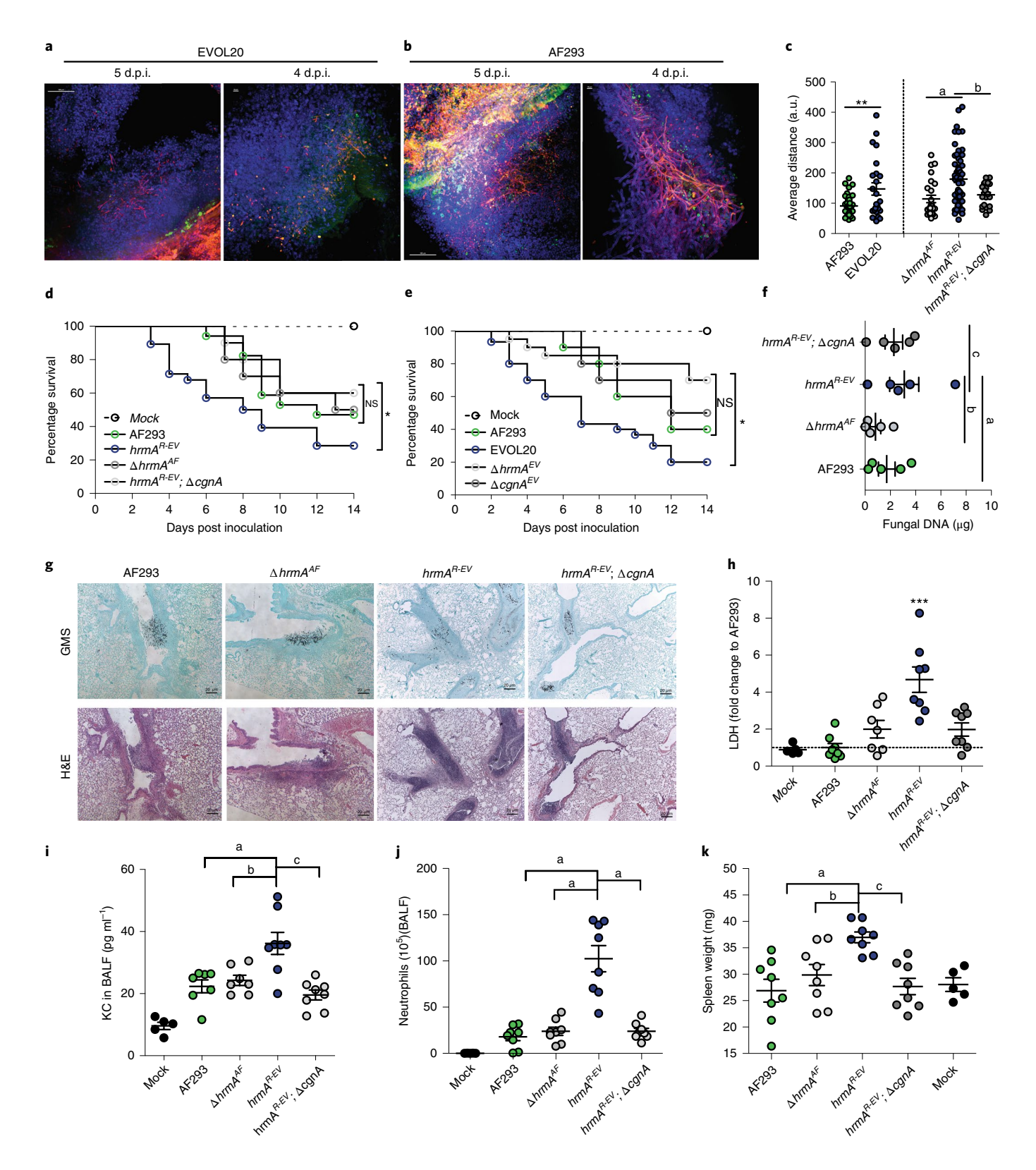
Fig. 6 | H-MORPH contributes to increased virulence through increased inflammation and diffuse lesion morphology. **a,b**, EVOL20^{tdtomato} (**a**) or AF293^{tdtomato} (**b**) murine lesions stained with DAPI and FITC-soy bean agglutinin. Scale bars: 4 d.p.i., 10 μm; 5 d.p.i.,100 μm. Results represent five independent animals from two independent preparations. **c**, Nearest-neighbour algorithm shows significantly increased distances between intralesion filaments in AF293 and EVOL20 (**P=0.0052) and $hrmA^{R-EV}$ (a, P=0.0003; b, P=0.0068) (AF293 n=45, EVOL20 n=24, $\Delta hrmA$ n=25, $hrmA^{R-EV}$ n=61, $hrmA^{R-EV}$; $\Delta cgnA$ n=22 biologically independent samples). One-way ANOVA with Sidak's multiple comparison test. **d**, $hrmA^{R-EV}$ (n=28 independent animals) is significantly more virulent (P=0.0346 by Gehan-Breslow-Wilcoxon test, GBW) than AF293 (n=16 independent animals) and $hrmA^{R-EV}$; $\Delta cgnA$ (n=10 independent animals, P=0.0417 by GBW). AF293 and $hrmA^{R-EV}$; $\Delta cgnA$ do not differ in virulence (NS: P=0.2087 by GBW). **e**, EVOL20 (n=30 independent animals) is significantly more virulent than $\Delta hrmA^{EV}$ (n=20 independent animals, P=0.0008 by GBW), $\Delta cgnA^{EV}$ (n=10 independent animals, P=0.0353 by GBW) and AF293 (n=10 independent animals, P=0.0465 by GBW). AF293, $\Delta hrmA^{EV}$ (P=0.1731 by GBW) nor $\Delta cgnA^{EV}$ (P=0.7812 by GBW) differ in virulence. **f**, $hrmA^{R-EV}$ does not increase fungal burden (a, P=0.4669; b, P=0.1322; b0, b0, b10 GBW) nor a20 independent animals each from two separate preparations) at 4 d.p.i. indicate a a3a4 d.p.i. indicate a a3a5 independent increase in cellular infiltrate in a4a4 d.p.i. indicate a a5a5 independent increase in cellular infiltrate in a6a6 independent animals each from two separate preparations) at 4 d.p.i. indicate a a5a6 has a fitter inoculation show increased LDH (a6, a6) and spleen weight (a6, a7) and spleen weight (a8, a8) one-way ANOVA with Dunnett's mult

Overexpression strains used the *A. nidulans gpdA* promoter for constitutive expression and this was introduced ectopically. Fluorescent strains expressing tdtomato were transformed with linear constructs of gpdA-driven tdtomato. Protoplasting was done with $Trichoderma\ harzianum$ (Sigma) lysing enzyme ^{33,34}. Strains were confirmed by Southern blotting as described previously ^{33,34}.

Growth and CM assays. Growth assays were performed as previously described 13 . Macroscopic morphology was quantified on GMM. A total 1,000 spores were spotted at the centre of the plates and grown for 72–96 h at 21% O_2 or 0.2% O_2 .

Representative images are of three biological replicates. Statistics were performed with one-way analysis of variance (ANOVA) with Tukey post test for multiple comparisons or two-tailed Students t-test. Error bars indicate s.e.m. centred at the mean. For shift experiments, cultures were started as described at 21% O_2 for 48 h, then shifted to 0.2% O_2 for 48 h.

Macroscopic morphology quantification. Colonies were imaged with a Canon PowerShot SX40 HS. In Fiji (ImageJ), images were converted to 8-bit. Colony perimeter was selected and a colour threshold was set to quantify percentage of the



colony that was 'white'. Furrows were counted by selecting only those that radiated away from the point of inoculation. A 'branched' furrow counted as a single furrow (Supplementary Fig. 1). The influence of oxygen on morphology was measured with a two-way ANOVA (GraphPad Prism).

RNA extraction and qrtPCR. Mycelia from liquid shaking cultures were flash frozen (~50 mg) and bead beaten for 1 min with 2.3 mm beads in 200 μ l of Trisure (Bioline Reagents). Homogenate was brought to a total volume of 1 ml of Trisure and RNA was extracted as previously described 31 . For RNA sequencing and qrtPCR, 50 ml cultures of 10^{6} spores ml $^{-1}$ were grown in normoxia (21% $\rm O_2$) at $37\,^{\circ}\rm C$ at $200\,\rm r.p.m.$ for $18\,h$ before being shifted to low oxygen (0.2% $\rm O_2$). When necessary, 25 ml culture was collected at $18\,h$ for the normoxia samples. For qrtPCR and RNA sequencing, $5\,\mu\rm g$ of RNA was DNase treated with Ambion Turbo DNAse (Life Technologies) according to the manufacturer's instruction. For qrtPCR DNase-treated RNA was processed as previously described 31 . The mRNA levels were normalized to actA and tub2 for all qrtPCR analyses. Statistical analysis for n>2 was performed with one-way ANOVA with Dunnet post test for multiple comparisons. Error bars indicate s.e.m. The qrtPCR data were collected on a CFX Connect Real-Time PCR Detection System (Bio-Rad) with CFX Maestro Software (Bio-Rad) and primer sequences are provided in Supplementary Table 9.

RNA sequencing and analysis. RNA sequencing and RNA library preparation were carried out by SeqMatic LLC. Briefly, DNase-treated RNA (400-600 ng l-1) were sent for QC using RNA Screen Tape Analysis (Agilent) and RNA library preparation using an Illumina TruSeq Standard mRNA library35 preparation kit with poly-A mRNA enrichment. RNA sequencing was performed as Illumina NextSeq High Output Run with single end reads at 1×75 base pairs (bp). Analysis of RNA-Seq was performed by aligning sequence reads to the annotated genome of A. fumigatus strain Af293 obtained from FungiDB (release 35)36 with GSNAP (2 December 2018) with splice-aware, single-ended mode³⁷. The alignments were processed with Picard (v.2.14.1) to clean, sort and assign read groups (tools CleanSam, AddOrReplaceReadGroups) (http://broadinstitute.github.io/picard/). Sequence read counts overlapping genes were computed with featureCount tool in the Subread package (v.1.6.2; ref. 38). The read count table was processed in R using the DESeq2 (v.3.8) to identify differentially regulated genes and generate heat maps. Pipeline BASH scripts for the alignment, read count pipeline and R analysis are available in the github repository (https://github.com/stajichlab/Afum_ RNASeq_hrmA; BioProject PRJNA551460). Heat map in Fig. 4 was drawn using collapsed replicates showing top DESeq2 with a P < 0.05 and log of differential expression >1 and a minimum FPKM (fragments per kilobase of transcript per million mapped reads) of 5. Heat map in Fig. 4 was drawn using collapsed replicates showing transcripts with computed expression value difference with an adjusted P < 0.05 and log of differential expression >1 and a minimum FPKM of 5. Heat map in Supplementary Fig. 5 was drawn showing all replicates and a P-value cutoff of 0.05 for genotype as an explaining variable for expression differences.

Surface attachment assays. Briefly, 10^4 spores seeded per well in a round-bottom 96-well polystyrene plate were incubated for $24\,\mathrm{h}$ at $37\,^\circ\mathrm{C}$ at ambient oxygen in 1% GMM. Wells were washed twice with water and stained for $10\,\mathrm{min}$ with 0.1% (wt/vol) crystal violet. Following two washes with water, remaining crystal violet was dissolved in 100% ethanol and absorbance was quantified at $600\,\mathrm{nm}$. For matrix complementation experiments, matrix donating strains were cultured in RPMI 1640 (Gibco) at 5×10^7 spores ml $^{-1}$ in $100\,\mathrm{m}$ for $24\,\mathrm{h}$ at $37\,^\circ\mathrm{C}$ at ambient oxygen. Cultures were filtered through Miracloth to remove fungus and supernatants were further filtered through a $0.22\,\mu\mathrm{m}$ PVDF sterile filter syringe. Filtered supernatants containing secreted GAG were diluted to 40% in fresh RPMI 1640 and used to perform the adherence assay with the attachment-deficient strain $\Delta uge3$.

Murine virulence assays. Survival. Female CD-1 outbred mice (Charles River Laboratory), 20–24 g were immune-suppressed with a single dose of triamcinolone acetonide (Kenalong-10, Bristol-Myer Squibb) at 40 mg kg $^{-1}$ 24 h before inoculation. Mice were inoculated with $10^{\rm 3}$ spores per 40 μ l of sterile PBS buffer as previously described 13,31 and monitored for end-point criteria. Kaplan–Meier curves were generated and log-rank Mantel–Cox tests and Gehan–Breslow–Wilcoxon tests were performed.

Histopathology, fungal burden and nearest-neighbour calculation. Lungs from mice immune-suppressed as described were harvested 4 d.p.i. Lungs were prepared for Gömöri methenamine silver and hematoxylin and eosin staining or fungal burden quantification as described³¹. A nearest-neighbour calculation was applied to Gömöri methenamine silver images³⁹. In Matlab (MathWorks), binary images were generated and filaments defined as objects. Lesions in airways were analysed blindly. Mean distances between each object in a lesion and its 30 nearest neighbours was calculated. For nearest-neighbour calculations four murine lungs were processed per experimental group with two histopathology slides prepared per animal. For fungal burden four to five animals were used per group.

FunPACT sample preparation. Lungs from mice immune-suppressed as described above were harvested on days 4 and 5 after inoculation. Lungs were harvested

and perfused with 1% paraformaldehyde and fixed for 24 h at room temperature. Following fixation, lobes of fixed lungs were separated with one lobe per 1.75 ml microcentrifuge tube. Lobes were washed with PBS and embedded in 4% (vol/vol) 29:1 acrylamide:bis-acrylamide (Bio-Rad) and 0.25% (wt/vol) VA-044 (Wako) in PBS 13 . To facilitate polymerization, tubes were left open at 0.2% O2 at 37 °C for 1h and then closed and incubated at 37 °C in a water bath for 4h. Embedded lobes were maintained at 4 °C or were processed for PACT tissue clearing. To clear the lobes, embedded lobes were trimmed of excess polymer and cut into 1 mm cubes using a stereomicroscope. Cubes were incubated in 20 ml of 8% (wt/vol) sodium dodecyl sulfate in PBS shaking at 150 r.p.m. at 37 °C for 6–8 weeks in the dark. When cubes became transparent, they were processed for staining and imaging.

After clearing, the cubes were washed three times with PBS for 1 h each. A subset of cubes was then transferred to a $1.75\,\text{ml}$ microcentrifuge tube and stained for 48 h with FITC-soy bean agglutinin at $20\,\mu\text{g}\,\text{ml}^{-1}$ (Vector Labs). Lectin-labelled cubes were washed in PBS for 24h to remove excess lectin and cubes were placed in a refractive index matching solution (40 g HistoDenz: Sigma, in 30 ml of PBS 40) with DAPI (10 $\mu\text{g}\,\text{ml}^{-1}$). Stained cubes in refractive index matching solution + DAPI were mounted on standard $24\times40\times1.5$ glass slides with a press-to-seal silicone isolator (Invitrogen: P247444).

Cellularity and immunological studies. Mice were immune-suppressed and inoculated as described above with eight mice per group. At 60 h after fungal inoculation, animals were killed using a lethal dose of pentobarbital and bronchoalveolar lavage was performed, then BALF and cells, lungs and spleens were collected. Cells from bronchoalveolar lavage and lungs were prepared for staining. Lung tissue was minced and digested with 2.2 mg ml-1 collagenase IV (Worthington), 1 U ml-1 DNase1 (Zymo Research) and 5% FBS at 37 °C for 45 min. BALF was centrifuged to isolate cells and suspended in red blood cell lysis buffer. Re-suspended cells from lung homogenate were also treated for red blood cell lysis. Cell numbers were enumerated with Trypan Blue staining. For cellularity analysis, the cells were stained with fixable viability dye (eFluor 780, eBioscience), anti-CD45 (Pacific orange, Invitrogen), anti-CD11b (PECy5, BioLegend), anti-Ly6G (FITC, BioLegend) and anti-SiglecF (BV421, BD bioscience), and then analysed on a MacsQuant VYB cytometer. The neutrophils were identified as CD45+Siglec F-Ly6G+CD11b+ cells and alveolar macrophages as CD45+SigletF+CD11bdim cells. Methods were adapted from Misharin et al. 41. Samples were run on a MacsQuant VYB cytometer and analysed with FlowJo v.9.9.6. The gating strategy is provided in Supplementary Fig. 16. BALF was used to quantify host cell damage and chemoattractant KC through the use of LDH-cytotoxicity colorimetric assay (BioVision no. K311) and Mouse CXCL1/KC DuoSet ELISA (R&D Systems no. DY453), respectively.

Fungal biofilm sample preparation. Biofilms for imaging were cultured in MatTek dishes (MatTek no. P35G-1.0-14-C) by seeding 10^5 spores ml⁻¹ of GMM with 2 ml per dish for 24 h at 37 °C with 5% CO₂ at 21% O₂ or 0.2% O₂. CFW stain (Sigma) was used to visualize the hyphae at a final concentration of 25 μ g ml⁻¹ for 15 min.

Fluorescent microscopy. Fluorescent confocal microscopy was performed on an Andor W1 Spinning Disk Confocal with a Nikon Eclipse Ti inverted microscope stand with Perfect Focus, a Zeiss LSM880 with two multi-alkali photomultiplier tubes, GaAsP detector and a transmitted light detector or a Zeiss LSM800 AxioObserver.

HrmA localization studies. Fungi were cultured on coverslips in GMM at 30 °C for 18 h until short hyphae, were washed, ultraviolet fixed, stained with $5\,\mu g\,ml^{-1}$ DAPI (Life Technologies) and mounted on slides. Images were acquired with a ×100 oil-immersion objective at 488 nm (GFP) and 405 nm (DAPI) on the Andor W1 Spinning Disk Confocal. Z-stacks were assembled in Fiji (ImageJ) with sum intensity projections. Images are representative of at least ten images. Quantification was performed as previously described⁴².

Fungal biofilm imaging and quantification. Biofilms were imaged in MatTek dishes with a ×20 multi-immersion objective (Nikon) or ×10 multi-immersion objective (Zeiss, C-Apochromat ×10/0.45 W M27) using water. CFW biofilms were imaged at 405 nm and tdtomato biofilms were imaged at 561 nm at depths from 300 to 500 nm. Three-dimensional projections were generated in Nikon NIS-Elements Viewer (Nikon) or Zeiss Blue (Zeiss). For quantification of biofilm architecture strains expressed tdtomato and were imaged on the Zeiss LSM880 AxioObserver with the exception of IFM 59356-1 and IFM 59356-3 which were stained with CFW (25 $\mu g\,ml^{\text{--}1}$). To quantify the branch length and branch density distribution of the hyphae network image stacks were processed in BiofilmQ (https://drescherlab. org/data/biofilmQ/) as follows. First, noise and background fluorescence where removed by local averaging, that is Tophat-filtering, respectively. Second, the hyphae structure was binarized by thresholding using Otsu's method⁴³. Third, the obtained data were skeletonized with a custom BiofilmQ analysis module and all branches above a threshold length were considered for further investigation. Visualization of branch features was performed in BiofilmQ.

FunPACT imaging. Mounted samples for funPACT were imaged on the Andor W1 Spinning Disk Confocal with a $\times 20$ multi-immersion objective lens used with oil or a $\times 40$ oil-immersion objective. Areas of fungal growth were identified by manual scanning at 561 nm. Lesions were imaged at 405, 488 and 561 nm at various depths. Images were processed in Nikon NIS-Elements Viewer for deconvolution and three-dimensions rendering.

Cell wall staining. Hyphae were generated as described for localization studies. Filaments were stained with 25 μ g ml $^{-1}$ CFW (Fluorescent Brightener 28, Sigma) for 15 min or soluble Dectin-1 as described previously⁴⁴. Ten hyphae images were processed per strain.

Scanning and transmission electron microscopy. Fungal biofilms for scanning and transmission electron microscopy were grown on 12 mm sterile glass coverslips in six-well plates for 24 h at 37 °C at 21% O_2 with 10^6 spores ml $^{-1}$ in RPMI 1640 (Gibco). Two coverslips were generated per sample. Samples were processed for SEM (scanning electron microscopy) through a critical point drying method. Briefly, media were removed and replaced with fixative (2% GTA/2% PF in 0.05 M sodium cacodylate at pH 7.4) for 15 min at room temperature. Fresh fixative was then added for 24 h. Coverslips were then washed three times (0.05 M sodium cacodylate at pH 7.4 for 5 min) and then incubated for 1 h at room temperature in 1% OsO₄ in 0.05 M sodium cacodylate before three washings as before. Samples were then ethanol dehydrated for 10 min in each 30%, 50%, 70% and 85% ethanol and were then washed three times in 100% ethanol. Coverslips were then transferred to a critical point drying holder and incubated in 100% hexamethyldisilazane twice for 10 min each. Samples were then mounted on SEM stubs and coated with osmium plasma coater (4 nm) and were stored in a desiccator before imaging. SEM images were acquired on an FEI (Thermo Fisher Scientific) Scios2 LoVac dual beam FEG/FIB scanning electron microscope with a Schottky emitter source. Images were acquired at 15.0 kV with 3 nm spot size.

Transmission electron microscopy and cell wall measurements. For transmission electron microscopy fungal biofilms were fixed in 5 ml of 2× fixative (2% GTA/2% PF in 0.05 M sodium cacodylate pH 7.4) for 1 h and then replaced with fresh fixative. Biofilms were scraped from coverslips and hyphae were pelleted and excess fixative removed. Hyphae were transferred to 100 µl of 2% molten agar and solidified. Agar drops were trimmed to removed excess agar and transferred to 1 ml of fresh fixative and rotated for 3 h at room temperature then 48 h at 4°C. Pellet was rinsed in 0.1 M sodium cacodylate/0.1 M sucrose to remove GTA and then postfix treated with 2% OsO4 in 0.1 M sodium cacodylate/0.07 M sucrose for 2h. Soft agar pellet was then rinsed twice with dH₂O and then transferred to En-bloc stain with 1% uranyl acetate for 2h at room temperature in the dark. Pellet was then dehydrated through ethanol series at room temperature with 30%, 50%, 70% for 30 min each, then on a rotator for 2 d, followed by further dehydration with 85% then 95% ethanol for 30 min and then 100% ethanol for six rinses over 6 h. Samples were then left at 4°C for 48 h. Samples were then incubated twice in propylene oxide for 30 min each, then immersed in 1:1 LX112 (LADD):PO for 1 h at room temperature and then in 1.5:1 LX112:PO for 18 h. LX112 from LADD epoxy solution was used in 6A:4B for medium hard block. Excess fluid was removed and samples were placed in vacuum desiccator for 24h before being transferred to BEEM capsules with fresh LX112, centrifuged for 30 min at 1500 r.p.m. and returned to vacuum desiccator for 12 h. Samples were polymerized at 45 °C for 24h, 60 °C for 24h and then cooled and thin sectioned and placed in 2% UA_{MeOH} for 10 min followed by 3% Reynolds lead citrate for 2-3 min. Protocol was based on Burghardt & Droleskey 45 . Samples were imaged on JEOL JEM 1010 transmission electron microscope at 100.0 kV. To determine cell wall size, ImageJ was used to open images files and for each cross-section of a filament ten measurements of cell wall thickness, disregarding the electron-dense extracellular matrix, were averaged per filament.

Statistics and reproducibility. All statistical analysis was performed in GraphPad Prism 5, GraphPad Prism 8 and R. Unless otherwise noted, all statistical analyses were performed with a minimum of three biologically independent samples. All images are representative of a minimum of three biologically independent samples that represent a minimum of three independent experimentations unless otherwise noted. The funPact images are representative of five independent animals but to reduce the use of animals, samples for funPact images were generated from two independent sample preparations. For comparisons between two groups two-tailed unpaired *t*-tests were performed. For comparisons between more than two groups one-way ANOVA with Tukey, Sidak or Dunnett post tests for multiple comparisons were performed. All error bars indicate s.e.m. centred around the mean.

Ethics statement. The National Research Council Guide for the Care and Use of Laboratory Animals was strictly followed for all animal experiments. The animal experiment protocol was approved by Institutional Animal Care and Use Committee at Dartmouth College (protocol: cram.ra.1)

Reporting Summary. Further information on research design is available in the Nature Research Reporting Summary linked to this article.

Data availability

RNA sequencing data that support the findings of this study have been deposited under NCBI Gene Expression Omnibus with the identifier GSE133440 under the BioProject PRJNA551460. The genomic sequencing data for EVOL20 and reference AF293 have been deposited under BioProject identifier PRJNA417720. All strains and any other data used to support these findings will be made available upon reasonable request to the corresponding author.

Code availability

The custom scripts that were used in this study are available at https://github.com/stajichlab/Afum_RNASeq_hrmA, https://github.com/stajichlab/Afum_hrmA_cluster_evolution, https://github.com/stajichlab/Afum_popgenome and https://github.com/stajichlab/Afum_EVOL20. The BiofilmQ software is available for public download at https://drescherlab.org/data/biofilmQ/. Other data that support the findings presented here are available upon request from the corresponding author.

Received: 19 December 2018; Accepted: 9 August 2019; Published online: 23 September 2019

References

- Slutsky, B., Buffo, J. & Soll, D. R. High-frequency switching of colony morphology in *Candida albicans. Science* 230, 666–669 (1985).
- Simpson, L. M., White, V. K., Zane, S. F. & Oliver, J. D. Correlation between virulence and colony morphology in *Vibrio vulnificus*. *Infect. Immun.* 55, 269–272 (1987)
- Kuthan, M. et al. Domestication of wild Saccharomyces cerevisiae is accompanied by changes in gene expression and colony morphology. Mol. Microbiol. 47, 745–754 (2003).
- Workentine, M. L. et al. Phenotypic heterogeneity of Pseudomonas aeruginosa populations in a cystic fibrosis patient. PLoS ONE 8, e60225 (2013).
- Haussler, S. et al. Highly adherent small-colony variants of *Pseudomonas aeruginosa* in cystic fibrosis lung infection. *J. Med. Microbiol.* 52, 295–301 (2003).
- Hagiwara, D. et al. Whole-genome comparison of Aspergillus fumigatus strains serially isolated from patients with aspergillosis. J. Clin. Microbiol. 52, 4202–4209 (2014).
- Fong, J. C. & Yildiz, F. H. The rbmBCDEF gene cluster modulates development of rugose colony morphology and biofilm formation in Vibrio cholerae. J. Bacteriol. 189, 2319–2330 (2007).
- Drenkard, E. & Ausubel, F. M. Pseudomonas biofilm formation and antibiotic resistance are linked to phenotypic variation. Nature 416, 740–743 (2002).
- Miller, M. G. & Johnson, A. D. White-opaque switching in *Candida albicans* is controlled by mating-type locus homeodomain proteins and allows efficient mating. *Cell* 110, 293–302 (2002).
- Workentine, M. L. et al. Phenotypic and metabolic profiling of colony morphology variants evolved from *Pseudomonas fluorescens* biofilms. *Environ. Microbiol.* 12, 1565–1577 (2010).
- Jain, N., Guerrero, A. & Fries, B. C. Phenotypic switching and its implications for the pathogenesis of *Cryptococcus neoformans*. FEMS Yeast Res. 6, 480–488 (2006).
- Jain, N., Hasan, F. & Fries, B. C. Phenotypic switching in fungi. Curr. Fungal Infect. Rep. 2, 180–188 (2008).
- Kowalski, C. H. et al. Heterogeneity among isolates reveals that fitness in low oxygen correlates with Aspergillus fumigatus virulence. MBio 7, e01515-16 (2016).
- Barker, B. M. et al. Transcriptomic and proteomic analyses of the Aspergillus fumigatus hypoxia response using an oxygen-controlled fermenter. BMC Genom. 13, 62 (2012).
- Kale, S. D. et al. Modulation of immune signaling and metabolism highlights host and fungal transcriptional responses in mouse models of invasive pulmonary aspergillosis. Sci. Rep. 7, 17096 (2017).
- McDonagh, A. et al. Sub-telomere directed gene expression during initiation of invasive aspergillosis. PLoS Pathog. 4, e1000154 (2008).
- 17. Fedorova, N. D. et al. Genomic islands in the pathogenic filamentous fungus Aspergillus fumigatus. PLoS Genet 4, e1000046 (2008).
- Law, M. J., Chambers, E. J., Katsamba, P. S., Haworth, I. S. & Laird-Offringa, I. A. Kinetic analysis of the role of the tyrosine 13, phenylalanine 56 and glutamine 54 network in the U1A/U1 hairpin II interaction. *Nucleic Acids Res.* 33, 2917–2928 (2005).
- Abdel-Nour, M. et al. The Legionella pneumophila collagen-like protein mediates sedimentation, autoaggregation, and pathogen-phagocyte interactions. Appl. Environ. Microbiol. 80, 1441–1454 (2014).
- Chen, S. M. et al. Streptococcal collagen-like surface protein 1 promotes adhesion to the respiratory epithelial cell. BMC Microbiol. 10, 320 (2010).
- Wang, C. & St Leger, R. J. A collagenous protective coat enables *Metarhizium anisopliae* to evade insect immune responses. *Proc. Natl Acad. Sci. USA* 103, 6647–6652 (2006).

- Gravelat, F. N. et al. Aspergillus galactosaminogalactan mediates adherence to host constituents and conceals hyphal beta-glucan from the immune system. PLoS Pathog. 9, e1003575 (2013).
- 23. Lee, M. J. et al. Deacetylation of fungal exopolysaccharide mediates adhesion and biofilm formation. *mBio* 7, e00252–00216 (2016).
- Brown, G. D. & Gordon, S. Immune recognition: a new receptor for beta-glucans. *Nature* 413, 36–37 (2001).
- 25. DePas, W. H. et al. Exposing the three-dimensional biogeography and metabolic states of pathogens in cystic fibrosis sputum via hydrogel embedding, clearing, and rRNA labeling. mBio 7, e00796-16 (2016).
- Yang, B. et al. Single-cell phenotyping within transparent intact tissue through whole-body clearing. Cell 158, 945–958 (2014).
- Chung, K. et al. Structural and molecular interrogation of intact biological systems. *Nature* 497, 332–337 (2013).
- Ballard, E. et al. In-host microevolution of Aspergillus fumigatus: a phenotypic and genotypic analysis. Fungal Genet. Biol. 113, 1–13 (2018).
- Gago, S., Denning, D. W. & Bowyer, P. Pathophysiological aspects of Aspergillus colonization in disease. Med. Mycol. 57, S219–S227 (2018).
- Morales, D. K. et al. Control of *Candida albicans* metabolism and biofilm formation by *Pseudomonas aeruginosa* phenazines. *mBio* 4, e00526–00512 (2013).
- Beattie, S. R. et al. Filamentous fungal carbon catabolite repression supports metabolic plasticity and stress responses essential for disease progression. *PLoS Pathog.* 13, e1006340 (2017).
- 32. Szewczyk, E. et al. Fusion PCR and gene targeting in *Aspergillus nidulans*. Nat. Protoc. 1, 3111–3120 (2006).
- Grahl, N. et al. In vivo hypoxia and a fungal alcohol dehydrogenase influence the pathogenesis of invasive pulmonary aspergillosis. *PLoS Pathog.* 7, e1002145 (2011).
- 34. Willger, S. D. et al. A sterol-regulatory element binding protein is required for cell polarity, hypoxia adaptation, azole drug resistance, and virulence in Aspergillus fumigatus. PLoS Pathog. 4, e1000200 (2008).
- 35. Love, M. I., Huber, W. & Anders, S. Moderated estimation of fold change and dispersion for RNA-seq data with DESeq2. *Genome Biol.* 15, 550 (2014).
- Basenko, E. Y. et al. FungiDB: an integrated bioinformatic resource for fungi and oomycetes. J. Fungi (Basel) 4, 39 (2018).
- Wu, T. D., Reeder, J., Lawrence, M., Becker, G. & Brauer, M. J. GMAP and GSNAP for genomic sequence alignment: enhancements to speed, accuracy, and functionality. *Methods Mol. Biol.* 1418, 283–334 (2016).
- Liao, Y., Smyth, G. K. & Shi, W. featureCounts: an efficient general purpose program for assigning sequence reads to genomic features. *Bioinformatics* 30, 923–930 (2014).
- Friedman, J. H., Bentely, J. & Finkel, R. A. An algorithm for finding best matches in logarithmic expected time. ACM Trans. Math. Softw. 3, 209–226 (1977).
- Treweek, J. B. et al. Whole-body tissue stabilization and selective extractions via tissue-hydrogel hybrids for high-resolution intact circuit mapping and phenotyping. *Nat. Protoc.* 10, 1860–1896 (2015).
- Misharin, A. V., Morales-Nebreda, L., Mutlu, G. M., Budinger, G. R. & Perlman, H. Flow cytometric analysis of macrophages and dendritic cell subsets in the mouse lung. Am. J. Respir. Cell Mol. Biol. 49, 503–510 (2013).
- Danhof, H. A. & Lorenz, M. C. The *Candida albicans* ATO gene family promotes neutralization of the macrophage phagolysosome. *Infect. Immun.* 83, 4416–4426 (2015).

- 43. Liao, P. S., Chew, T. S. & Chung, P. C. A fast algorithm for multilevel thresholding. *J. Inf. Sci. Eng.* 17, 713–727 (2001).
- Shepardson, K. M. et al. Hypoxia enhances innate immune activation to *Aspergillus fumigatus* through cell wall modulation. *Microbes Infect.* 15, 259–269 (2013).
- Burghardt, R. C. & Droleskey, R. Transmission electron microscopy. Curr. Protoc. Microbiol. 3, 1–39 (2006).

Acknowledgements

We thank J. Obar (Dartmouth) for his helpful comments, A. Lavanway and L. Howard (Dartmouth) for their microscopy expertise, T. J. Smith for graphical model design and construction, D. Limoli for funPACT assistance, S. Dhingra for tool development (plasmids), D. Carter-House for assistance with DNA extraction for whole genome sequencing and S. Lockhart, S. Howard, and D. Hagiwara for sharing A. fumigatus isolates. This work was supported by the efforts of R.A.C. through funding by NIH National Institute of Allergy and Infectious Diseases (NIAID) (grant nos. R01AI130128 and 2R01AI081838). R.A.C holds an Investigators in Pathogenesis of Infectious Diseases Award from the Burroughs Wellcome Fund. C.H.K. was supported by the Molecular and Cellular Biology Training Grant at Dartmouth (no. 5T32 GM 8704-20, principal investigator: D. Compton) from the National Institute of General Medical Sciences from July 2016 to June 2018 and the NIH NIAID Ruth L. Kirschstein National Research Service Award (no. F31AI138354) from July 2018. C.D.N. is supported by the National Science Foundation (grant no. MCB 1817342), a Burke Award from Dartmouth College, a pilot award from the Cystic Fibrosis Foundation (grant no. STANTO15RO) and NIH grant no. P20-GM113132 to the Dartmouth BioMT COBRE. Data analyses were performed on the UC Riverside High-Performance Computational Cluster supported by grant nos. NSF DBI-1429826 and NIH S10-OD016290.

Author contributions

C.H.K. designed, performed and analysed most of the experiments and wrote the manuscript. J.D.K. performed the histopathology quantification and assisted with funPact analysis. K.L. performed the cellularity analysis. M.C.B. assisted with fluorescent microscopy analysis. R.H. generated software for biofilm analysis. C.D.N. generated software for biofilm analysis and performed the biofilm analysis. J.E.S. performed analysis on genomic and RNA sequencing and phylogenetic analysis. R.A.C. designed experiments, supervised the study and edited the manuscript. All authors reviewed and approved the manuscript.

Competing interests

The authors declare no competing interests.

Additional information

Supplementary information is available for this paper at https://doi.org/10.1038/s41564-019-0558-7.

Reprints and permissions information is available at www.nature.com/reprints.

Correspondence and requests for materials should be addressed to R.A.C.

Publisher's note Springer Nature remains neutral with regard to jurisdictional claims in published maps and institutional affiliations.

© The Author(s), under exclusive licence to Springer Nature Limited 2019



Corresponding author(s):	Robert Cramer
Last updated by author(s):	08/08/2019

Reporting Summary

X Life sciences

Nature Research wishes to improve the reproducibility of the work that we publish. This form provides structure for consistency and transparency in reporting. For further information on Nature Research policies, see <u>Authors & Referees</u> and the <u>Editorial Policy Checklist</u>.

Statistics					
For all statistical analys	es, confirm that the following items are present in the figure legend, table legend, main text, or Methods section.				
n/a Confirmed					
The exact sample size (n) for each experimental group/condition, given as a discrete number and unit of measurement					
A statement of	A statement on whether measurements were taken from distinct samples or whether the same sample was measured repeatedly				
The statistical test(s) used AND whether they are one- or two-sided Only common tests should be described solely by name; describe more complex techniques in the Methods section.					
A description of all covariates tested					
A description of any assumptions or corrections, such as tests of normality and adjustment for multiple comparisons					
A full description of the statistical parameters including central tendency (e.g. means) or other basic estimates (e.g. regression coefficient AND variation (e.g. standard deviation) or associated estimates of uncertainty (e.g. confidence intervals)					
For null hypothesis testing, the test statistic (e.g. <i>F</i> , <i>t</i> , <i>r</i>) with confidence intervals, effect sizes, degrees of freedom and <i>P</i> value noted Give <i>P</i> values as exact values whenever suitable.					
For Bayesian analysis, information on the choice of priors and Markov chain Monte Carlo settings					
For hierarchic	For hierarchical and complex designs, identification of the appropriate level for tests and full reporting of outcomes				
Estimates of effect sizes (e.g. Cohen's <i>d</i> , Pearson's <i>r</i>), indicating how they were calculated					
Our web collection on <u>statistics for biologists</u> contains articles on many of the points above.					
Software and c	ode				
Policy information abou	ut <u>availability of computer code</u>				
Data collection	Nikon NIS-Elements Viewer (Nikon) software, Bio-Rad CFX Maestro, Zeiss Black, MACSQuant VYB				
Data analysis	Nikon NIS-Elements Viewer, FIJI (ImageJ), GraphPad Prism 5, MatLab, R, BiofilmQ, Zeiss Blue, FlowJo version 9.9.6				
For manuscripts utilizing custom algorithms or software that are central to the research but not yet described in published literature, software must be made available to editors/reviewers. We strongly encourage code deposition in a community repository (e.g. GitHub). See the Nature Research guidelines for submitting code & software for further information.					
Data					
- Accession codes, un - A list of figures that	ut <u>availability of data</u> include a <u>data availability statement</u> . This statement should provide the following information, where applicable: ique identifiers, or web links for publicly available datasets have associated raw data restrictions on data availability				
	e associated raw data: Figure S4, Figure S1, Figure 4, Figure 1. Following the final draft of the manuscript accession numbers to the raw h accession numbers and doi addresses provided. These data include genome sequencing and RNA-sequencing.				
Field-speci	fic reporting				

Please select the one below that is the best fit for your research. If you are not sure, read the appropriate sections before making your selection.

Ecological, evolutionary & environmental sciences

Behavioural & social sciences

Life sciences study design

All studies must dis	close on these points even when the disclosure is negative.	
Sample size	Power analysis was performed to determine sample size for animal experiments (survival etc.)	
Data exclusions	Data were excluded from animal studies when mice were sacrificed due to symptoms of central nervous system (CNS) infection. These exclusions were based on the pre-established criteria that mice suffering from CNS infection present different pathologies than those with pulmonary infections. A replicate for hrmAR-EV in hypoxia for the RNA-sequencing was excluded due to poor RNA quality and PCA plot indicating that this sample did not cluster with the other replicates.	
Replication	All attempts at replication were successful. FunPACT was not replicated with these exact samples because of the use of animal lives and the 10-12 week period of sample processing, however n=5 were utilized for each experimental group and were accumulated from two separate sample preparations/processings.	
Randomization	For animal studies, mice were randomly sorted (by groups of 4 or 5) into experimental or mock groups. For in vitro fungal assays no randomization was performed.	
Blinding	Blinding was use in the replication of all animal studies and in the analysis of histopathology samples and fluorescent fungal biofilms. Blinding	

Reporting for specific materials, systems and methods

We require information from authors about some types of materials, experimental systems and methods used in many studies. Here, indicate whether each material, system or method listed is relevant to your study. If you are not sure if a list item applies to your research, read the appropriate section before selecting a response.

IVI	ateriais & experimental systems	ivie	tnods
n/a	Involved in the study	n/a	Involved in the study
	Antibodies	\boxtimes	ChIP-seq
\boxtimes	Eukaryotic cell lines		Flow cytometry
\boxtimes	Palaeontology	\boxtimes	MRI-based neuroimaging
	Animals and other organisms		
\times	Human research participants		
\times	Clinical data		

was not used in other in vitro fungal assays.

Antibodies

The antibodies used in the paper were bought from eBioscience, Invitrogen, Biolegend and BD bioscience: Antibodies used Fixable Viability Dye (eFluor™ 780, eBioscience, 65-0865-14) anti-CD45 (Pacific orange, Invitrogen, Clone 30-F11, MCD4530) anti-CD11b (PECy5, BioLegend, Clone M1/70, 101209) anti-Ly6G (FITC, BioLegend, Clone 1A8, 127605) anti-SiglecF (BV421, BD bioscience, Clone E50-2440, 562681) Validation The antibodies were validated based on the datasheet provided by the manufacturers.

Animals and other organisms

Policy information about studies involving animals; ARRIVE guidelines recommended for reporting animal research Charles River CD-1 outbred female mice 6-8 weeks (20-24 grams). Laboratory animals Wild animals The study did not involve wild animals Field-collected samples The study did not involve field-collected samples. Clinical samples were published previously and provided by those laboratories. The National Research Council Guide for the Care and Use of Laboratory Animals was strictly followed for all animal experiments. Ethics oversight The animal experiment protocol was approved by Institutional Animal Care and Use Committee (IACUC) at Dartmouth College

Note that full information on the approval of the study protocol must also be provided in the manuscript.

Flow Cytometry

Plots

Confirm that:

- The axis labels state the marker and fluorochrome used (e.g. CD4-FITC).
- The axis scales are clearly visible. Include numbers along axes only for bottom left plot of group (a 'group' is an analysis of identical markers).
- All plots are contour plots with outliers or pseudocolor plots.
- A numerical value for number of cells or percentage (with statistics) is provided.

Methodology

Sample preparation

The lungs were minced in the digestion buffer containing PBS, 2.2 mg/ml Collagenase IV (Worthington), 1U/ml DNasel (Zymo research) and 5% FBS and were incubated in 37 °C for 45 minutes. The suspended cells from BAL and lungs were treated with RBC lysis buffer and enumerated with Trypan blue staining.

Instrument MacsQuant VYB cytometer

Software FlowJo version 9.9.6

Cell population abundance The isolated cells from BAL and lung were sufficient for antibody staining and data analysis.

Gating strategy The gating strategies were the same as the supplementary figure.

Tick this box to confirm that a figure exemplifying the gating strategy is provided in the Supplementary Information.